*Bulletin de la Société Royale des Sciences de Liège, Vol. 74, 5-6, 2005*

# Pupil remapping to achieve high dynamic range imaging

S. Lacour & G. Perrin

[1]LESIA, Observatoire de Paris Meudon, France

**Abstract:** Correction of the influence of phase corrugation in the pupil plane is a fundamental issue in achieving high dynamic range imaging. We present here an imaging system which, thanks to non-redundant pupil remapping and spatial filtering, allows a perfect calibration of the Optical Transfer Function. We do show that such a system would be free from phase perturbations, photon noise limited, and would allow processed imaging with high dynamic range.

## 1 Introduction

Real-time adaptive optics systems become a more and more common feature of imaging system. The technique was first developed on ground-based telescopes to achieve high resolution imaging, and enjoyed considerable success. As a result, it is now spreading to new fields like high contrast imaging for space telescopes (TPF will use active optics) or retina imaging in opthalmology. However, one must not forget other techniques that utilize post-detection data processing. They have the advantage of being either a complement or a replacement to correct further away the technological limits of real-time compensation. Speckle imaging (Labeyrie 1070), as well as aperture masking (Haniff et al. 1987), are the two best known techniques in astronomy. The principle is to recover the Fourier components of the target by using sequences of short (time-wise the perturbations) exposures. Although both methods have also enjoyed considerable success, they both suffer from inherent limitations — incoherent redundancies in speckle imaging depress heavily the modulation transfer function (MTF), and aperture masking uses only a tiny fraction of the light coming through the telescope.

One solution to these problems is a remapping of the pupil. A fundamental advantage of breaking the "golden rule" (Traub 1986) is the ability to transform a redundant entrance pupil into a non-redundant exit one. Single mode fibers now give us the technology for such a massive modification of the geometry of the pupil, while keeping zero optical path difference. In addition, they also provide perfect spatial mode filtering. Data collection and analysis are then similar to those utilized for aperture masking, with the noticeable advantage of having flux from the whole entrance pupil, and the possibility to completely disentangle instrumental from astrophysical information.

# 2 PRINCIPLE OF PUPIL REMAPPING

## 2.1 Image deconvolution

A single telescope pupil can be considered as an interferometric array. Each pair of coherent patches ($i$,$j$) in the pupil selects only one specific spatial frequency described by a frequency vector $\mathbf{u}_k$; where $\mathbf{u}_k = (\mathbf{r}_i - \mathbf{r}_j)/(\lambda f)$ and where $\mathbf{r}_i$ and $\mathbf{r}_j$ are the location of the $i$th and $j$th patch. Each patch will interfere in the image plane (at focal distance $f$), and if no coherence loss exist, the fringe visibility will be a complex number $V_k$ which is a measurement of the Fourier component of the object at frequency $\mathbf{u}_k$.

Following such an interferometric approach, one can "discretize" the perturbations. Providing a small enough division step, the transfer function of each patch is a phase ($\phi_i$) due to atmospheric piston, and a gain ($g_i$) due to scintillation. Therefore, atmospheric perturbation is equivalent to $M$ (one for each patch) complex transmission numbers $P_i = g_i \exp(\imath\phi_i)$. The resulting optical transfer's function (OTF) at the frequency $\mathbf{u}_k$ is :

$$\sum_{(i,j)\epsilon\beta_{i,j}} P_i P_j^\star, \tag{1}$$

where $\beta_{i,j}$ is the set of baseline vectors for which $\mathbf{u}_k = (\mathbf{r}_i - \mathbf{r}_j)/(\lambda f)$. Hence, the image Fourier component at this frequency is :

$$\mu_k = V_k \sum_{(i,j)\epsilon\beta_{i,j}} P_i P_j^\star. \tag{2}$$

Deconvolution requires the knowledge of the $M$ complex terms $P_i$, but since each observable $\mu_k$ is dependent of an unknown $V_k$, disentangling atmospheric from astronomical information is impossible. The solution usually adopted is to average the $\sum_{(i,j)\epsilon\beta_{i,j}} P_i P_j^\star$ terms, in complex or module depending on the amplitude of the phase perturbations. Here, we are proposing an instrument in the following section which allows determination of this term at any moment, and without previous knowledge of the visibility terms $V_k$.

## 2.2 Pupil remapping

The main point is that the complex visibilities $V_k$ only depend on the baselines $\mathbf{u}_k$. They do not change with a possible rearrangement of the patches (Tallon & Tallon, 1992).

The concept is shown in Figure 1. Entrance sub-apertures collect independently the radiation from an astronomical source, and focus the light onto the input head of a single-mode optical fiber ($\mathbf{r}_i$ is the location vector of the $i$th sub-aperture). The radiation is then guided by the fibers down to a recombination unit, in which the beams are rearranged into a 2D non-redundant configuration (of location vector $\mathbf{r'}_i$). Correlation between the rearranged beams occurs by the way of a classical Michelson stellar interferometer; fringes at frequency $\mathbf{u'}_l = (\mathbf{r'}_i - \mathbf{r'}_j)/(\lambda f)$ in the image plane are a measurement of the Fourier component given by the entrance baseline vector $(\mathbf{r}_i - \mathbf{r}_j)/(\lambda f)$. Note the uniqueness of this baseline thanks to non-redundant remapping. The Fourier components of the image are now given by the –simple– relation :

$$\mu_l = V_k P_i P_j^\star. \tag{3}$$

Note again that the complex visibilities $V_k$ are dependent on the entrance baseline $\mathbf{u}_k$, and not on the exit baselines $\mathbf{u'}_l$ . This last property has its importance since it allows to resolve the indetermination. Providing $M$ sub-aperture and $R$ redundant entrance baselines, the numbers

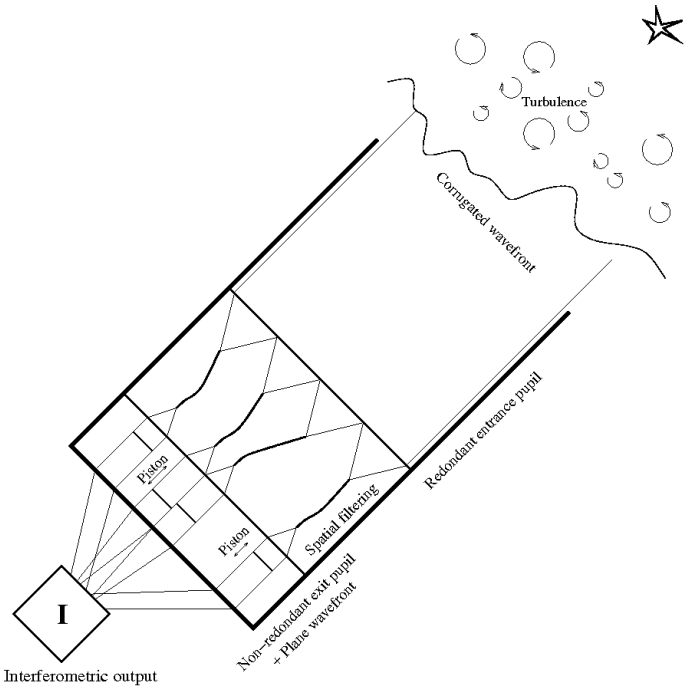


Figure 1: Conceptual design of a remapped pupil interferometer using single-mode fibers

of complex unknowns are of $M*(M-1)/2-R$ visibilities, and $M-1$ transmission factors. On the other hand, the measurements are $M*(M-1)/2$ $\mu_l$. Hence, if $R > M-1$, we have enough information to resolve the unknowns, and an –almost– reversible problem.

The concept is more easily understood in a specific case. Figure 2 is a sketch of a pupil subdivided into 5 distinct parts. On the left panels are the complex transmission of the discretized pupil. The central panels show the Fourier transform of the image. In the upper panel, the $\mu_k$ terms are the optical transfer function factor the Fourier transform of the object, but this is not the case with a remapped pupil. The equations linking the observables $\mu_k$ and $\mu_l$ to the unknown $P_i$ and $V_k$ are clarified in the upper and lower right panels. They correspond to Equations 2 and 3 respectively. Inverting the upper sets of equations is impossible since the number of unknowns is higher than the number of measurements. On the other hand, we can demonstrate that the second set of equations has a solution by using the log of Equation 3. It becomes

$$\ln(|\mu_l|) + \imath\Phi(\mu_l) = \ln(|V_k|) + \ln(g_i) + \ln(g_j) + \imath(\Phi(V_k) + \phi_i - \phi_j), \tag{4}$$

where $\Phi()$ is the phase function, and $g_i$, $g_j$, $\phi_i$ and $\phi_j$ are defined in Section 2.1. The problem can therefore be reduced into two set of linear equations, one for the amplitudes (i.e. $\ln(|\mu_l|) = M_A.[\ln(|V_k|), \ln(g_i)]$), and one for the phases (i.e. $\Phi(\mu_l) = M_P.[\Phi(V_k), \phi_i]$). $M_A$ and $M_P$ are two matrix containing only 1,0, and -1 values. For example, Equation 5 is the phase equation, featuring matrix $M_P$. The rank of this matrix is 8, while the number of unknown is 11. The three terms of degeneracy are : one for the absolute phase reference, and two for the tip and tilt. Thus, providing additional information on these three terms, we can perform a singular value decomposition on the matrix and obtain from the measurements $\mu_l$ both the phase perturbations and the phase of the object visibilities. The conclusion is similar with the amplitudes, except that there is no tip and tilt information required.

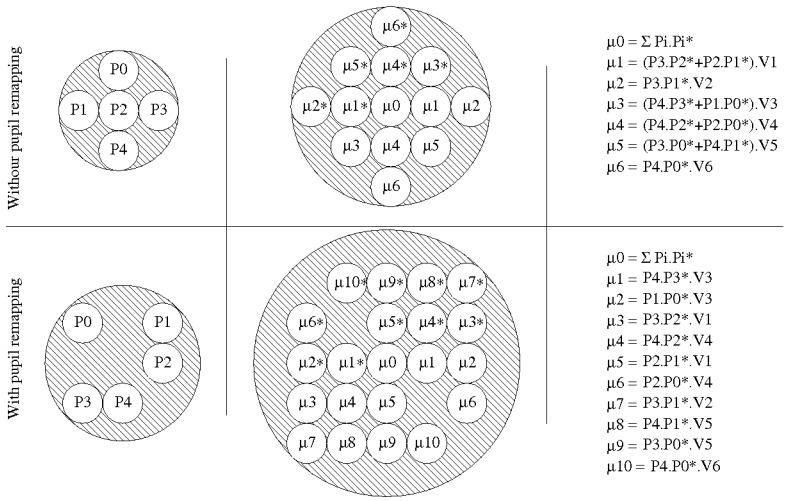


Figure 2: Effect of pupil remapping on the Fourier transfer of the image (see Section 2.2).

$$\begin{bmatrix} \Phi(\mu_1) \\ \Phi(\mu_2) \\ \Phi(\mu_3) \\ \Phi(\mu_4) \\ \Phi(\mu_5) \\ \Phi(\mu_6) \\ \Phi(\mu_7) \\ \Phi(\mu_8) \\ \Phi(\mu_9) \\ \Phi(\mu_{10}) \end{bmatrix} = \begin{pmatrix} 0 & 0 & 1 & 0 & 0 & 0 & 0 & 0 & 0 & -1 & 1 \\ 0 & 0 & 1 & 0 & 0 & 0 & -1 & 1 & 0 & 0 & 0 \\ 1 & 0 & 0 & 0 & 0 & 0 & 0 & 0 & -1 & 1 & 0 \\ 0 & 0 & 0 & 1 & 0 & 0 & 0 & 0 & -1 & 0 & 1 \\ 1 & 0 & 0 & 0 & 0 & 0 & 0 & -1 & 1 & 0 & 0 \\ 0 & 0 & 0 & 1 & 0 & 0 & -1 & 0 & 1 & 0 & 0 \\ 0 & 1 & 0 & 0 & 0 & 0 & 0 & -1 & 0 & 1 & 0 \\ 0 & 0 & 0 & 0 & 1 & 0 & 0 & -1 & 0 & 0 & 1 \\ 0 & 0 & 0 & 0 & 1 & 0 & -1 & 0 & 0 & 1 & 0 \\ 0 & 0 & 0 & 0 & 0 & 1 & -1 & 0 & 0 & 0 & 1 \end{pmatrix} . \begin{bmatrix} \Phi(V_1) \\ \Phi(V_2) \\ \Phi(V_3) \\ \Phi(V_4) \\ \Phi(V_5) \\ \Phi(V_6) \\ \phi_0 \\ \phi_1 \\ \phi_2 \\ \phi_3 \\ \phi_4 \end{bmatrix} \tag{5}$$

## 2.3 Dynamic range

Hence, by using a simple inversion program, the image would give measurements of perfectly calibrated complex Fourier components of our object. The advantage is straightforward. In classical imaging, phase and amplitude errors create speckles in the image plane, therefore limiting the dynamic range. In our instrument, statistical error due to the photon noise will be the only limiting factor, and therefore visibility error can be roughly estimated by a Gaussian noise $V/\delta V = \sqrt{N_p}/M$ . Thanks to Baldwin and Haniff (2002) equation of the dynamic range, we can estimate it for the reconstructed image by :

$$dyn = \sqrt{\frac{n_{vis}}{(\delta V/V)^2 + (\delta\phi)^2}} \approx \sqrt{\frac{M(M-1)}{M^2/N_p}} \approx \sqrt{N_p}\,, \tag{6}$$

where $n_{vis}$ is the total number of visibility data, $M$ the number of sub-divisions of the entrance pupil, and $N_p$ the total number of photon collected.

Simulations were performed to test this analytical result. In our example, a circular pupil is subdivided into 1 000 sub-apertures remapped into a non-redundant configuration. From it, 4 000 independent spatial frequencies are measured. Phases are obtained through phase closure, and tip and tilt taken equal to 0. The field of view (FOV) is limited to the Airy disk of the

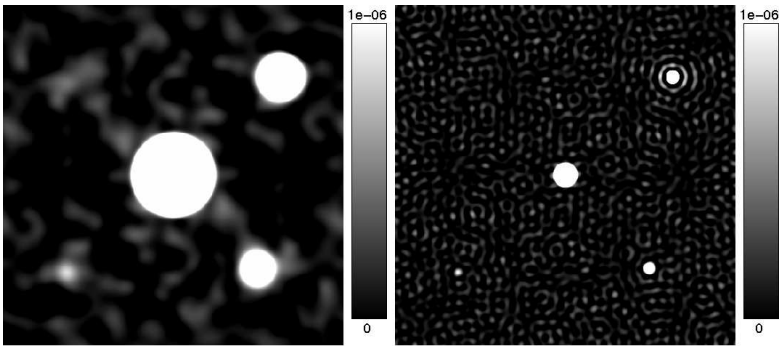


Figure 3: Reconstructed image from the knowledge of the complex visibilities, as they would be obtained with an instrument featuring a remapping of the pupil into several thousands independent frequency vectors (see Section 2.3). The three companions have a brightness of $10^{-4}$, $10^{-5}$, and $10^{-6}$ clockwise. The left image was obtained through a direct apodization of the visibilities, at the price of a reduction of the resolution (by a factor 4). The image on the right shows high dynamic range diffraction limited imaging, obtained with a reconstruction algorithm estimating the higher spatial frequencies. Both image are photon noise limited and have dynamic range of $7 \times 10^6$.

individual sub-apertures, and the resolution by the diameter of the telescope. Photon noise was incorporated to correspond to $10^{14}$ photons detected ($\delta V/V \approx 10^{-4}$). Another advantage of post-detection data processing is that it allows to use different image reconstruction algorithm, with a free choice of point spread function (PSF). Because we want a spatially limited PSF, we chose to apodize the frequency plane by a Gaussian function with a standard deviation $\sigma = \lambda/4D$ ($D$ is the diameter of the telescope). Such numerical apodization of the transfer function is in fact very similar to what is done instrumentally in apodized pupils (Kuchner & Traub 2002; Guyon 2003) and does show similar aptitudes: left image of Figure 3 has the dynamic range predicted by Equation 6, but at the cost of a considerable decrease in resolution — the factor 4 between $\sigma$ and $\lambda/D$. However, numerical processes in image restoration offer tools to retrieve higher missing frequencies, thus allowing softer apodization. We managed to obtain in the right image of Figure 3 a diffraction limited image — Gaussian apodization function with $\sigma = \lambda/D$ — and a dynamic range of $7 \times 10^6$ by using the Maximum Entropy Method (Narayan & Nityananda 1986). A movie is available as on-line material showing the progressive reconstruction of the image (http://fuse.pha.jhu.edu/˜lacour/10.7.gif.gz).

# References

A. Labeyrie, 1970, A&A 6, 83
C. A. Haniff, C. D. Mackay, D. J. Titterington, D. Sivia, and J. E. Baldwin, 1987, Nature 328, 694
W. A. Traub, 1986, Appl. Opt. 25, 528
M. Tallon and I. Tallon-Bosc, 1992, A&A 253, 641
J. E. Baldwin and C. A. Haniff, 2002, Phill. Trans. R. Soc. Lond. 360, 969
M. J. Kuchner and W. A. Traub, 2002, ApJ 570, 900
O. Guyon, 2003, A&A 404, 379
R. Narayan and R. Nityananda, ARA&A 1986, 127